



THE UNIVERSITY *of* EDINBURGH

Edinburgh Research Explorer

Vulnerability of Antarctica's ice shelves to meltwater-driven fracture

Citation for published version:

Lai, C-Y, Kingslake, J, Wearing, M, Cameron Chen, P-H, Gentine, P, Li, H, Spergel, JJ & van Wessem, JM 2020, 'Vulnerability of Antarctica's ice shelves to meltwater-driven fracture', *Nature*.
<https://doi.org/10.1038/s41586-020-2627-8>

Digital Object Identifier (DOI):

[10.1038/s41586-020-2627-8](https://doi.org/10.1038/s41586-020-2627-8)

Link:

[Link to publication record in Edinburgh Research Explorer](#)

Document Version:

Peer reviewed version

Published In:

Nature

General rights

Copyright for the publications made accessible via the Edinburgh Research Explorer is retained by the author(s) and / or other copyright owners and it is a condition of accessing these publications that users recognise and abide by the legal requirements associated with these rights.

Take down policy

The University of Edinburgh has made every reasonable effort to ensure that Edinburgh Research Explorer content complies with UK legislation. If you believe that the public display of this file breaches copyright please contact openaccess@ed.ac.uk providing details, and we will remove access to the work immediately and investigate your claim.



Vulnerability of Antarctica's ice shelves to meltwater-driven fracture

Ching-Yao Lai^{1*}, Jonathan Kingslake^{1,2}, Martin G. Wearing³, Po-Hsuan Cameron Chen⁴, Pierre Gentine⁵, Harold Li⁶, Julian J. Spergel^{1,2}, J. Melchior van Wessem⁷

[1] Lamont-Doherty Earth Observatory, Columbia University, Palisades, NY, USA

[2] Department of Earth and Environmental Sciences, Columbia University, New York, NY, USA

[3] School of Geosciences, University of Edinburgh, Edinburgh, UK

[4] Google Research, Mountain View, CA, USA

[5] Department of Earth and Environmental Engineering, Columbia University, New York, NY, USA

[6] Department of Computer Science, Columbia University, New York, NY, USA

[7] Institute for Marine and Atmospheric Research Utrecht, Utrecht University, Utrecht, the Netherlands

*cylai@ldeo.columbia.edu

Atmospheric warming threatens to accelerate the retreat of the Antarctic Ice Sheet by increasing surface melting and facilitating ‘hydrofracturing’¹⁻⁷, where meltwater flows into and enlarges fractures, potentially triggering ice-shelf collapse^{3-5,8-10}. The collapse of ice shelves that ‘buttress’¹¹⁻¹³ the ice sheet accelerates ice flow and sea-level rise¹⁴⁻¹⁶. However, we do not currently know if and how much of the buttressing regions of Antarctica’s ice shelves are vulnerable to hydrofracture if inundated with water. Here we provide two lines of evidence suggesting that many buttressing regions are vulnerable. First, we train a deep convolutional neural network (DCNN) to map the surface expressions of fractures in satellite imagery across all Antarctic ice shelves. Second, we develop a fracture stability diagram based on linear elastic fracture mechanics (LEFM) to predict where basal and dry surface fractures form under today’s stress condition. We find close agreement between the theoretical prediction and the DCNN-mapped fractures, despite limitations associated with detecting fractures in satellite imagery. Finally, we use the LEFM theory to predict where surface fracture would become unstable if filled with water. Many regions regularly inundated with meltwater today are resilient to hydrofracturing - stresses are low enough that all water-filled fractures are stable. Conversely, 60% \pm 10% of ice shelves (by area) both buttress upstream ice and are vulnerable to hydrofracture if inundated with water. The DCNN-map confirms the presence of fractures in these buttressing regions. Increased surface melting¹⁷ could trigger hydrofracturing if it leads to water inundating the widespread vulnerable regions we identify. These are regions where atmospheric warming may have the largest impact on ice-sheet mass balance.

Where ice shelves – the floating extensions of ice sheets – are laterally confined they generate resistive stress and transmit this upstream to slow the flow of ice into the ocean. This is called buttressing. Areas with larger tensile resistive stresses^{2,18} provide less buttressing^{13,19}. When buttressing ice shelves collapse, upstream glaciers accelerate^{14–16}. Observations and models have linked ice-shelf collapse to surface melting^{4,5,8,10,20} through hydrofracture; where meltwater flows into surface fractures, imposing additional loading and driving unstable fracture growth^{1,2}. Repeated hydrofracture close to an ice-shelf edge has been hypothesized as a potential mechanism to drive collapse⁴. Flexural stresses generated by the filling and draining of lakes on ice shelves may also facilitate hydrofracture and trigger collapse^{5,21,22}. Although hydrofracture has so far only been included in ice-sheet models with simple parametrizations^{9,10}, simulations predict it could accelerate the collapse of the Antarctic Ice Sheet in response to atmospheric warming^{9,10}.

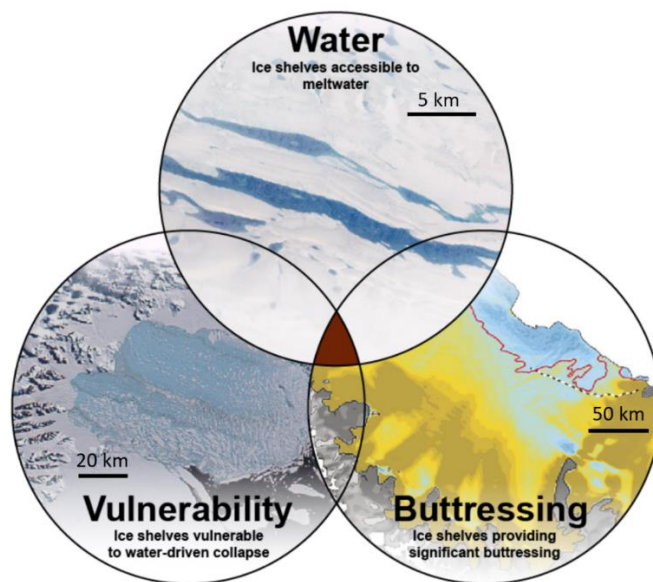


Figure 1 | Conceptualizing the regions of Antarctic ice shelves that will control the ice sheet's response to atmospheric warming. Circles represent ice-shelf regions (upper) where meltwater accumulates, (lower-left) that are vulnerable to hydrofracture if covered in meltwater, and (lower-right) where significant buttressing is generated. Images show: (upper) Amery Ice Shelf with water accumulated in large melt ponds, Feb 21, 1989, Landsat 4, NASA; (lower-left) the collapse of Larsen B Ice Shelf, Mar 7, 2002, MODIS, NASA; (lower-right) modelled estimate of buttressing on Larsen C Ice Shelf (Fürst et al. (2016)¹³; reproduced from their Fig. 3). Regions downstream of the red contour (blue) are relatively unimportant for buttressing.

Antarctica's response to surface melting

Hydrofracture requires sufficient surface meltwater and tensile stress. However, not all parts of ice shelves provide substantial buttressing and thus, to predict the impact of atmospheric warming on Antarctic ice loss we must predict (1) the distribution of meltwater on ice shelves^{7,17,23–25}; (2) the regions of ice shelves providing buttressing^{13,19}; and (3) the regions of ice shelves that will undergo hydrofracture if meltwater accumulates (Fig. 1; ref. ²⁶). Progress has been made in constraining where meltwater accumulates today and will in the future (the upper circle in Fig. 1). Stokes et al. (2019)²⁵ comprehensively mapped lakes in East Antarctica using satellite imagery from Jan 2017. Trusel et al. (2015)¹⁷ predicted that melt rates seen in areas that have undergone catastrophic collapse in the past will become widespread this century. Alley et al. (2018)⁷ assessed the state of firn on ice shelves, which is linked to the ability of an ice shelf to retain surface water²⁷, using microwave backscatter observations. They found some locations already in a state that would allow lake formation and potentially hydrofracture^{7,27}. However, a location will only undergo hydrofracture if local stresses allow, with higher tensile stress promoting hydrofracture. For clarity, here we will refer to the tendency of a location to hydrofracture if inundated with water as its *vulnerability to hydrofracture*. Crucially, areas of higher tensile stress² provide less buttressing^{13,19}, yet are most vulnerable to hydrofracture. Therefore, an important open question is: are any of the regions generating substantial buttressing also vulnerable to hydrofracture under present-day conditions? Do the two lower circles in Fig. 1 overlap? This is the focus of this article.

Fractures detection by a neural network

Fracture-like features are visible in satellite imagery (e.g., the 125m-resolution MODIS mosaic of Antarctica, MOA 2009²⁸; Fig. 3a), but comprehensive manual mapping is impractical (ice shelves cover 1.5 million pixels in MOA). Therefore, we employ a deep convolutional neural network (DCNN), the U-Net²⁹, to identify the fracture-like features in the relatively low resolution, but continent-wide MOA imagery. We trained the DCNN with a subset of MOA imagery in which fracture features were manually labeled (Extended Data Fig. 1c). The output of the DCNN is a map of the likelihood (ranging from 0 to 1) that a pixel contains part of a fracture. The trained DCNN performs well when evaluated against an unseen subset of imagery (Extended Data Fig. 2). We apply the trained DCNN to map fracture-like features across all of Antarctica's ice-shelves (Fig. 2). Examples of the imagery and the fracture features identified by the DCNN are shown in Fig. 3a and b respectively. Because there are morphological similarities between surface fractures and other fracture features – e.g., full-thickness rifts, surface expressions of basal fractures^{30–32} – it is likely that some of these make up a proportion of the fractures mapped by the DCNN. We refer to them throughout as fractures, but consider this limitation when comparing the DCNN results to the theoretical predictions below.

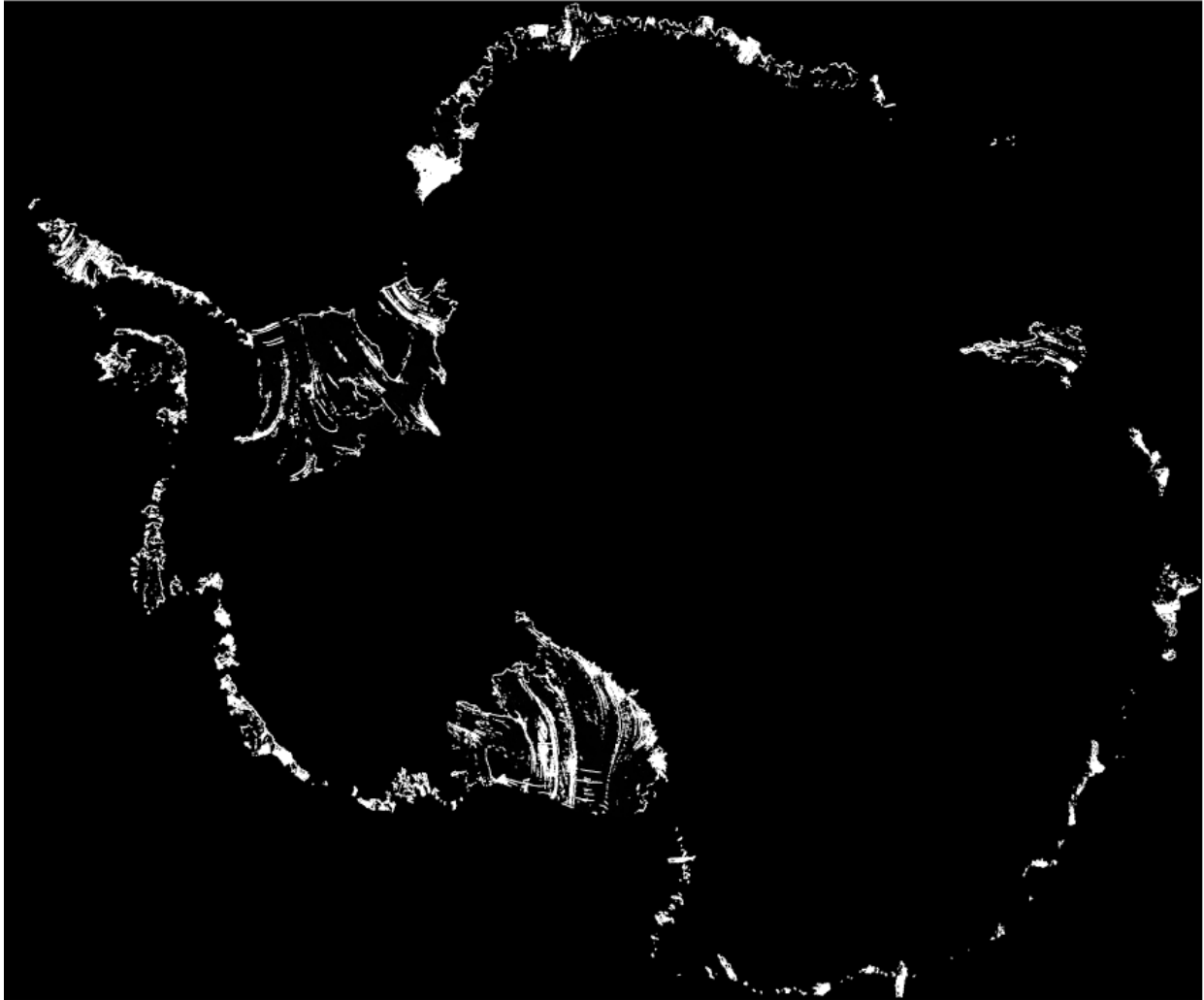


Figure 2 | Continent-wide fracture map. Locations of fracture features classified by the U-Net are marked in white. The model (learning rate = 1.4, momentum = 0.2, decay rate = 0.95) and threshold (= 0.2) that optimize the model performance on the validation set are chosen to generate the fracture map. The performance of the U-Net evaluated against the unseen testing set: AUC = 0.97, sensitivity = 0.63 and specificity = 0.99 (percentage of pixels without fracture not classified as fracture by DCNN).

Fracture stability diagram

Next, we develop a new theoretical framework to predict the location of dry surface fractures. There are two widely-adopted models for ice fracturing: the zero-stress approximation³³ and linear elastic fracture mechanics (LEFM)^{2,34}. The zero-stress approximation only applies where fractures are densely spaced (fracture spacing is much smaller than fracture depth)³⁵. Because the spacing between dry fractures (~1 km) is often larger than the fracture depth, we apply LEFM. Although dry-fracture depths predicted by LEFM are simply a factor of $\pi/2$ larger than those predicted by the zero-stress approximation¹ (Extended

Data Fig. 5b), LEFM provides an estimate of the critical tensile resistive stress required to form dry fractures, which is crucial for this study.

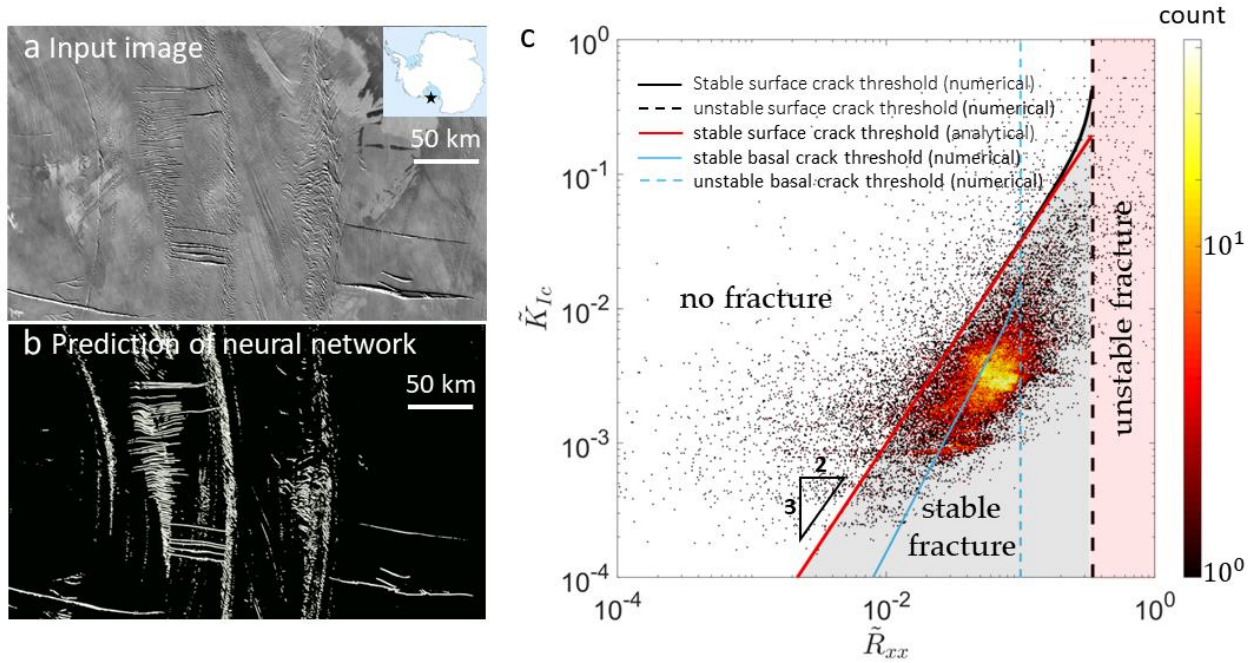


Figure 3 | Model-observation comparison of fracture locations. (a) 125m-resolution MOA showing part of the Ross Ice Shelf (location shown by star in inset) and the (b) fracture features (marked in white) identified by the DCNN with good performance (AUC = 0.97; Methods). (c) Stability diagram for dry surface fractures and basal fractures; dimensionless stress \tilde{R}_{xx} against dimensionless toughness \tilde{K}_{Ic} . The boundary between the no-fracture and stable-fracture regions is obtained numerically (black and blue curve for surface and basal fracture, respectively) and analytically (red curve for surface fracture, equation 2). Dashed lines denote the boundary between stable and unstable fractures. Dimensionless stress and toughness (equation 1) are computed for every fracture location detected by the DCNN and displayed as a density plot (~32k data points); the colour bar denotes the number of fracture locations that have the same dimensionless values (Methods).

To quantify how ice-shelf stress affects fracture stability we construct a fracture stability diagram (Fig. 3c). Vertical propagation of a stable fracture stops when it is too energetically costly to break the ice further. In contrast, unstable fractures propagate through the entire ice thickness. Fractures may form on both the surface and base of ice shelves, their stability depends on the tensile resistive stress R_{xx} (ref. ^{2,34}) perpendicular to the fracture, ice thickness H , fracture toughness K_{Ic} (a measurable material property; ref. ³⁶) and ice density ρ_i . The stability of both surface and basal fractures depends on two fundamental parameters (Supplementary Information (SI) Section 3), the dimensionless tensile resistive stress (\tilde{R}_{xx}) and dimensionless fracture toughness (\tilde{K}_{Ic}):

$$\tilde{R}_{xx} \equiv \frac{R_{xx}}{\rho_i g H}, \quad \tilde{K}_{Ic} \equiv \frac{K_{Ic}}{\rho_i g H^{3/2}}. \quad (1)$$

We analytically derive a power-law (SI Section 3) for the critical tensile resistive stress R_{xx}^* that allows the formation of stable surface fractures (red curve in Fig. 3c),

$$\tilde{K}_{Ic} = \alpha \tilde{R}_{xx}^{*3/2}, \quad \alpha \equiv \frac{\pi}{3\sqrt{3}} \frac{F^{3/2}}{f^{1/2}}, \quad (2)$$

which closely matches the corresponding numerical solution (black solid curve in Fig. 3c; SI Section 3). When $R_{xx} < R_{xx}^*$, no surface fractures can exist according to LEFM (white area in Fig. 3c). When the dimensionless tensile resistive stress exceeds a threshold (black dashed line in Fig. 3c) surface fractures are unstable. The transition boundaries (between no-fracture, stable-fracture and unstable-fracture) for basal fractures with the inclusion of the effects of vertically varying temperature (SI Section 7) are shown by light blue curves in Fig.3c. In the absence of meltwater, LEFM predicts that a basal fracture will destabilize at a smaller dimensionless stress \tilde{R}_{xx} than a surface fracture.

To assess where the DCNN-identified fracture features lie in this space, we compute the dimensionless parameters, \tilde{R}_{xx} and \tilde{K}_{Ic} , for every fracture location (1 km resolution) using observed ice thickness³⁷, fracture toughness, $K_{Ic} = 150 \text{ kPa}\cdot\text{m}^{1/2}$, from laboratory measurements³⁶, strain rates derived from a data-constrained flow model¹³, and ice viscosity calculated using ice-surface temperature from a regional climate model³⁸ (Extended Data Fig. 6c). Fig. 3c plots them on the parameter space as a density map. Most fracture features (89% of 32k locations identified as fractures by the DCNN) lie in the parameter region where the theory predicts stable surface fractures (gray area in Fig. 3c). We also note that 56% of the 32k identified fracture features lie in the parameter regime of stable basal fractures. Given the simplicity of the theory and the limitations of the DCNN mapping, this agreement is encouraging and suggests that the theory predicts both stable surface and basal fractures across realistic ranges of \tilde{R}_{xx} and \tilde{K}_{Ic} . Note that no parameters were tuned to determine the locations of data on Fig. 3c.

Vulnerability to unstable hydrofracture

To estimate vulnerability to hydrofracture across all ice shelves, we next examine the extreme case when water inundates all ice shelves. In this way we estimate the geographic extent of the lower-left circle in Fig. 1. When surface fractures are filled with meltwater, the weight of water can destabilize the fractures, leading to unstoppable fracture propagation. However, when the ice stresses are sufficiently compressive, pre-existing water-filled fractures remain stable (SI Section 5). Here we assume that surface water flows rapidly into surface fractures and does not refreeze fast enough to affect fracture propagation. Slow inflow and refreezing could stabilize surface fractures. A fracture model coupled to a hydrological model could account for this³⁹.

In regions where $R_{xx} > R_{xx}^*$, (red in Fig. 4a), surface fractures will be unstable if filled with water – these locations are vulnerable to hydrofracture. Where $R_{xx} < R_{xx}^*$ water-filled fractures will be stable, unless the original dry fracture is deeper than d_i (Fig. 4a). The pre-existing surface fracture depth d_i required to destabilize hydrofracture increases as R_{xx} decreases, as plotted in Extended Data Fig. 5c-d. Given that pre-existing fractures in regions of low R_{xx} are unlikely to be 50-150 metres deep, we consider the ice-shelf regions marked yellow and green in Fig. 3 to be resilient to meltwater-driven fracturing. Finally, some regions have sufficiently compressive stresses that water-filled fractures cannot grow, regardless of their size (black regions in Fig. 4a).

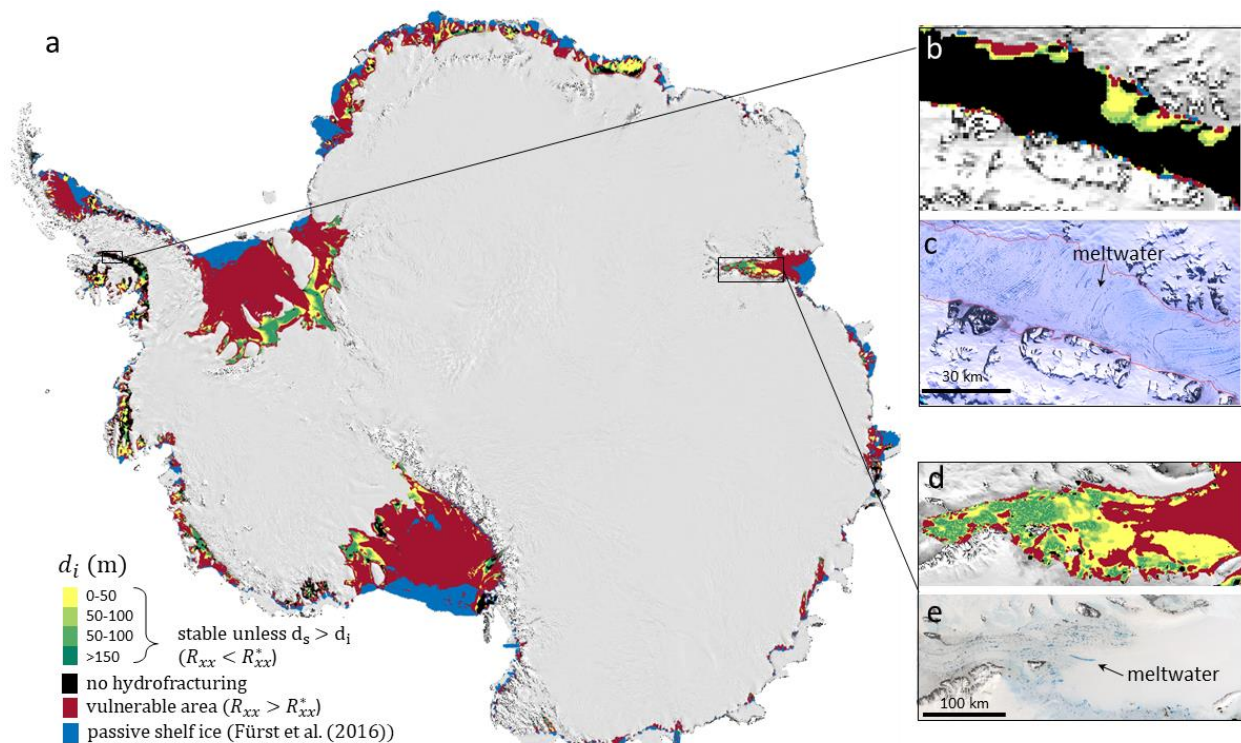


Figure 4 | Map of ice-shelf vulnerability to hydrofracture. (a) Water-filled fractures are unstable in vulnerable areas (red & blue) and stable in resilient regions (yellow & green) unless pre-existing surface fractures of depth d_i exist. Where stresses are sufficiently compressive, water-filled fractures cannot open (black). Present-day meltwater on the (c) Amery (Jan 15/17, 2019, Landsat 8) and (e) George VI (Feb 4, 1991, Landsat 5) ice shelves predominantly lies in regions resilient to hydrofracture (yellow, green & black in (b,d)). Blue denotes regions providing insignificant buttressing¹³. We find that $60\% \pm 10\%$ of the Antarctic ice shelf area provides buttressing and is vulnerable to hydrofracture (red).

Vulnerable and buttressing regions

Our key question is whether regions vulnerable to hydrofracture coincide with buttressing regions (Fig. 1). Both the DCNN-mapped fractures and the LEFM theory suggest they do coincide. Blue areas in Fig. 4a were identified by Fürst et al. (2016)¹³ as regions of ‘passive ice’ that provide little buttressing. Red regions in Fig. 4 are where the ice shelf is vulnerable to hydrofracture according to our LEFM analysis and also provide significant buttressing¹³; i.e., they lie outside of Fürst et al.’s passive regions. These regions cover $60\% \pm 10\%$ of the total area of Antarctica’s ice shelves. The details of the extent of these regions depend on the buttressing computation¹³ and the method used to compute stresses, but the finding that buttressing and vulnerable regions substantially overlap does not (Extended Data Fig. 8). The DCNN map confirms widespread surface fractures in these regions (Fig. 2).

While it does not impact our key conclusions, we neglect the impact of the low-density, low-viscosity near-surface firn layer, and ice softening due to damage (Methods). The net effect of the firn is to slightly increase surface fracture depths (SI Section 2, Extended Data Fig. 3c) and therefore slightly increase the extent of the vulnerable regions. Conversely, damaged ice would generate lower tensile resistive stress and decrease the extent of vulnerable regions slightly (Methods Section 3.3).

Hydrofracture can only occur if the ice-shelf surface is inundated with meltwater. In many locations large meltwater ponds have persisted for decades. Many of these, for example on the George VI (Fig. 4c), Amery (Fig. 4e), and Roi Baudoin ice shelves^{23,40} lie in regions that, due to low tensile (and in places compressive) resistive stresses, are resilient to hydrofracture (Fig. 4b,d). Moreover, using a recent survey of East Antarctic supraglacial lakes (Stokes et al., 2019)²⁵, we estimate an upper bound of only 0.6% of East Antarctic ice shelves (by area) currently provide buttressing, experience meltwater ponding, and are vulnerable to hydrofracture (Methods Section 4; Extended Data Fig. 10). Increased meltwater ponding in resilient locations will not lead to widespread hydrofracturing according to our analysis. However, predictions of future melt^{17,41} suggest that melt rates seen in locations which experience meltwater ponding today could become widespread by 2100 under high emissions scenarios. This, coupled with present-day widespread low porosity firn⁷ and large-scale surface-meltwater drainage that can transport water long distances from melt zones²⁶, strongly indicates that meltwater ponding could spread to many of the buttressing and vulnerable regions under future warming scenarios.

Summary

We have used fracture mechanics, machine learning and continent-wide datasets to estimate the vulnerability of Antarctica’s ice shelves to hydrofracture. Although hydrofracture and buttressing are favoured by different stress conditions, a large proportion of Antarctic ice shelves are both vulnerable to

hydrofracture, if inundated with meltwater, and provide significant buttressing. Our analysis yields a fracture stability diagram based on LEFM which shows promising agreement with the first continent-wide attempt at mapping fracture features, but could be extended to include viscous³⁵ and thermal effects³⁹. This theory could be implemented into an ice-sheet model to improve sea-level predictions and the machine learning approach to mapping fractures can easily be applied to higher-resolution imagery. If warming allows meltwater to enter the vulnerable, buttressing regions we have identified, hydrofracture-driven ice-shelf collapse is possible, which could have major consequences for Antarctic mass loss and global sea-level rise.

Methods

1. Machine learning development and evaluation

To develop a machine learning model to detect the fracture patterns, we first train several models on a training set to learn the relationships between input images and corresponding fractures labeled manually by visual inspection. Next, we assess the performance of the trained models on a validation data set with a range of hyperparameters. The best performing model on the validation data is selected for evaluation on an unseen test data set.

1.1. Training, validation, and testing datasets

A 1000 x 1000 km (8000 x 8000 pixels, at 125m-resolution) region covering the Larsen C and George VI ice shelves in the MODIS mosaic of Antarctica (MOA^{28,42}) was used as the training and validation sets (Extended Data Fig. 1a). This subset of MOA contains fracture features near shear margins, calving fronts, and grounding lines, covering the range of typical fracture patterns observed on Antarctic ice shelves. We first crop the 8000 x 8000 pixels image into smaller tiles (1000 x 1000 pixels), of which 32 tiles contain ice-shelves (non-black areas in Extended Data Fig. 1a). We randomly divide the 32 tiles into a training set (26 image tiles) and a validation set (6 image tiles). To evaluate the developed machine learning model on an unseen data set, we prepare an independent testing set consisting of 6 image tiles of size 1000 x 1000 pixels randomly selected from the remaining continent-wide MODIS image.

Using a Matlab script, we manually label the datasets (38 tiles in total) by visually identifying fractures based on their linear morphology and alignment perpendicular to flow (fractured areas are filled in white as shown in Extended Data Fig. 1c). The marked fractures are rasterized as binary labels. A sample training tile and its labels are shown in Extended Data Fig. 1b and c, respectively.

1.2. Model selection

For model selection, here we compare the predictive performance of a wide range of machine learning models. We explored four sets of models, including (1) several single layer convolutional neural networks (CNN) with different filter sizes, 1×1 , 28×28 , and 56×56 , (2) U-Net²⁹ using different numbers of first layer feature maps (1, 2, 4, 16, 32, 64), (3) Feature Pyramid Networks (FPN)⁴³ with a ResNet-18 backbone, and (4) an edge detector⁴⁴ (using OpenCV's cv.Canny implementation with minimal threshold = 0 and maximum threshold = 255). There are many other advanced segmentation models such as DeepLabv3⁴⁵, SegNet⁴⁶, PSPNet⁴⁷, etc. Doing a detailed comparison for a wide range of advanced segmentation models to detect fractures on satellite imagery is an interesting future direction to explore.

We use the area under the receiver operating characteristics curve (AUC) as the evaluation metric for model selection. The AUCs of the trained models on the validation set is plotted in Extended Data Fig. 2a(i) as a function of the total number of parameters in each model. All models were trained with a batch size of 1. The single-layer CNN and FPN models were trained using the stochastic gradient descent optimizer to minimize the cross-entropy loss. The U-Net was trained with the momentum optimizer to minimize the cross-entropy loss.

As shown in Extended Data Fig. 2a, the performance of U-Net increases significantly when the initial number of feature maps (d) increases from 1 to 4, reaching a maximum of AUC = 0.99 when $d = 32$, then slightly decreases when d goes beyond 32. Single-layer CNN with filter sizes of 1×1 , 28×28 , and 56×56 perform well but do not exceed the performance of U-Net when the number of parameters is increased. This is likely due to insufficient number of layers to recognize complex fracture patterns. Lastly, the FPN was a state-of-the-art method for recognizing objects on the COCO dataset⁴⁸, however, it has an AUC of 0.82 for the fracture detection task in this study, which is significantly lower than U-Net's. This is likely a result of overparameterization for this comparatively simpler task. Based on these observations, we selected U-Net with 32 initial feature maps for making predictions on the continent-wide map. A sample validation label and image are displayed in Extended Data Fig. 2 c and d, respectively.

1.3. U-Net architecture

To detect fractures we employed the U-Net²⁹, a DCNN that has been successfully applied to image segmentation. In addition to a contracting path, which is typical for convolutional neural networks, the U-Net also contains an expansive path, which gives rise to its U-shaped architecture (Extended Data Fig. 1d). The expansive path recovers the location of the classified pattern and enables efficient use of training examples.

In our U-Net setup, there are 2 classes (fracture and non-fracture) in the output predictions, one channel in the input image (1000 x 1000 pixels), 32 feature maps in the first layer, and 13 convolutional layers (ten 3×3 convolutional layers, two 2×2 transposed convolutional layers, and one final 1×1 convolutional layers) in the entire architecture (Extended Data Fig. 1d). For each block in the contracting path the image is convolved twice with 3×3 filters, each followed by a ReLU activation function, and down-sampled with a 2×2 max pooling (stride 2) filter. For each block in the expansive path, the image size is increased by a 2×2 up-sampling (transposed convolutional) filter, followed by a concatenation with the cropped feature maps from the corresponding contracting layer, two 3×3 convolution filters and a ReLU activation function. The number of filters is halved and doubled in the down-sampling and up-sampling steps,

respectively. Finally, a 1x1 convolution is applied to generate the output prediction (960 x 960 pixels). We train our model using the momentum optimizer with the hyperparameters (learning rate = 1.4, momentum = 0.2, decay rate = 0.95) that optimize the AUC on the validation set. A sample prediction of the fracture is shown in the right panel of Extended Data Fig. 1d.

1.4. Threshold selection

Next, a classification threshold is applied to the predictions (continuous output between 0 to 1, Extended Data Fig. 2e) so that every pixel is classified as either a fracture (white in Extended Data Fig. 2f) or non-fracture (black in Extended Data Fig. 2f). Every threshold corresponds to a point on the receiver operating characteristics (ROC) curve. Lower thresholds yield higher sensitivity (percentage of pixels with fractures that are classified as fractures) but lower specificity (percentage of pixels without fractures that are classified as non-fractures). We apply a range of thresholds (0-1) on the validation-set predictions and measure the F1 scores. The threshold (= 0.2) with the highest F1 score on the validation set is selected for generating the continent-wide fracture map shown in Fig. 2.

1.5. Evaluation on testing set

Finally, we evaluate the model performance using the testing set which has not been seen by the model. The model shows an AUC of 0.97 (95% CI: 0.93-0.99) on the testing set, as shown in Extended Data Fig. 2b. Confidence interval (CI) of model performance is calculated using bootstrapping with 1000 samples. We further perform a data titration experiment to understand the impact of the training set size with respect to the performance. Increasing the number of training tiles from 6 to 26 only increases the AUC from 0.95 to 0.97, indicating that increasing the training dataset size further will likely not significantly improve performance. The classification performance on the testing set, after applying the classification threshold (= 0.2) to the predictions, shows a specificity of 0.99 and sensitivity of 0.63.

1.6. Continent-wide fracture map

We apply the final U-Net with the selected threshold to the continent-wide MOA imagery to identify fracture features across all ice shelves (marked in white in Fig. 2). Note that the resolution of the fracture map is 125 m, but the resolution of the strain rate data (Extended Data Fig. 6a) is 1 km.¹³ We downsample the fracture map to 1 km resolution to construct Fig. 3c using the fracture locations and strain rate data on the same grid. The downsampling algorithm uses nearest-neighbor interpolation. The images before and after downsampling are shown in Extended Data Fig. 2f and g, respectively. Some detailed fracture patterns are lost in the 1km-resolution fracture map (Extended Data Fig. 2g) but the overall fracture

distribution is retained. For future work, the proposed method can be extended to a finer grid where higher resolution imagery (e.g., Landsat) and strain rates are available⁴⁹.

1.7. Limitations in fracture identification

Most (89%) of the fractures mapped using 125m-resolution MOA imagery lie in the region of stability diagram (dimensionless tensile resistive stress and dimensionless fracture toughness) where our theory predicts that the tensile resistive stress exceeds the critical value required for dry surface fracturing. The remaining fracture locations fall in the region of parameter space where the theory predicts no dry surface fractures should form. There are several possible explanations, for example, unresolved locally high strain rates, existing fractures advecting into lower stress regions, incorrectly identified fractures, or fracturing resulting from more complex fracture modes than our theory describes.

The theory also predicts that dry surface fractures exist in many locations where the DCNN does not detect them. Several explanations for this are possible. First, the satellite imagery we utilize operates in a part of the electromagnetic spectrum where energy does not penetrate through snow and ice. Therefore, it will fail to detect surface fractures buried by snow unless it has a sufficient surface expression. For example, the presence of buried surface fractures can sometimes be inferred from the presence of elongated depressions in the snow surface, which may be observable in MOA. However, it is possible that many sub-surface fractures are not detected by the DCNN because they have little or no surface expression. Satellite-based radar (e.g., RADARSAT, SENTINEL-1) can detect sub-surface structures because radio waves penetrate up to ~10 m into the sub-surface^{50,51}. Applying the DCNN to these data may allow us to test whether buried surface fractures are widespread in these regions, as predicted by the theory. Secondly, it is possible that the limitations of the DCNN are causing us to fail to detect surface fractures in these locations. Although the performance of the DCNN output prediction (a continuous variable ranging from 0 to 1) evaluated against testing set is excellent (AUC=0.97), the binary classification of fracture features (a binary variable, either 0 or 1) identified via application of a classification threshold yields a sensitivity of 0.63, indicating that 37% of all fracture features manually labelled on the test data are not detected by the DCNN. Performance of the U-Net is expected to improve if higher resolution imagery were used. It is also possible that the relatively low-resolution imagery is incapable of detecting crevasses smaller than a few hundred metres in length or width, and we are therefore failing to detect many smaller crevasses in the locations where the theory predicts they should form. Future work could apply the DCNN within a high-performance computer framework to higher resolution imagery.

2. Theory of ice-shelf fractures

We have developed a model of ice-shelf fracturing based on Linear Elastic Fracture Mechanics (LEFM). A complete theoretical description is available in the SI, which draws on references ^{1,2,18,33–36,52–57}. The SI describes LEFM for surface crevasses (section 1) and basal crevasses (section 6), the determination of dimensionless parameters (equation 1) for the surface fracture stability diagram (Fig. 3c), the derivation of the critical stress required for surface crevasse formation (equation 2) (section 3), firm effects on surface crevasses (section 2), surface crevasse depth from LEFM vs Nye's zero-stress approximation (section 4), water-filled crevasse stability and initial flaws (section 5), and the effects of vertical englacial temperature gradients on surface and basal fractures (section 7). Using theoretical results derived in the SI we discuss the stability of surface and basal fractures below.

2.1. Physical regimes of surface and basal fractures

The stability diagram for surface and basal fractures is shown in Extended Data Fig. 4d. We have labeled physical regimes I-V on the stability diagram, marked the ice-shelf locations corresponding to each regime (Extended Data Fig. 4e-h), and quantitatively showed the percentage of ice shelves corresponding to each physical regime I-V. The four panels (Extended Data Fig. 4e-h) show the variability in the location of each regime when different ice-shelf stress datasets are used (their corresponding stability diagrams are shown in Fig. 3c and Extended Data Fig. 8). Locations where basal fractures are stable (blue; regime III) cover 41-62% of ice shelves and are theoretically dominant on ice shelves. Locations where surface fractures could theoretically form are widespread and overlap with that of stable and unstable basal fractures. The locations of unstable basal fractures (red; regime IV) cover only 2-4% of the total ice-shelf area. These red areas largely overlap with areas of high extensional stress downstream of pinning points where ice is damaged or near existing rifts, as shown in Extended Data Fig. 4e-h, with close-view examples shown in the second row of panel e-h. Note that the red area is purely an output from a given dimensionless stress input, and is independent of the neural network-mapped fracture-feature locations (white locations).

Within this 2-4% area (regime IV; red in Extended Data Fig. 4e-h) the effective viscosity could be overestimated in locations with highly damaged ice. Some red areas that coincide with fracture features disappear when Fürst et al.'s stress field¹³ is used directly (Extended Data Fig. 4g,h), as this product inherently includes the damage-induced softening of the ice. On the other hand, LEFM may be unable to accurately describe basal fracture stability. For example, ice may be more ductile⁵⁸ at the base and thus require more energy to break than predicted by LEFM, thus stabilizing basal crevasses that would be unstable according to LEFM and reducing the red areas in Extended Data Fig. 4e-h.

3. Data used for the fracture stability diagram

3.1. Data sources

The parameters required to plot ice-shelf locations on the stability diagram of dimensionless tensile resistive stress and dimensionless fracture toughness are tensile resistive stress R_{xx} , ice thickness H , fracture toughness K_{Ic} , and ice density ρ_i . The stress is calculated using the strain rate $\dot{\epsilon}_{xx}$ and the effective viscosity, which is calculated using the viscosity factor B , according to Glen's flow law, $R_{xx} = 2B\dot{\epsilon}_{xx}^{1/n}$. We use the along-flow strain rate $\dot{\epsilon}_{xx}$ (Extended Data Fig. 6a) determined from a model assimilation of satellite-derived velocity data^{13,59}. The assimilated velocity field effectively smooths the observed velocity field⁶⁰, which otherwise can be problematic when differentiating to compute strain-rate fields⁶¹. An alternative approach is to use the 1st principal strain rate. In the next section we demonstrate that using the 1st principal stress instead of the along-flow stress does not impact our main conclusions. Ice-shelf thickness is from Bedmap2³⁷ (Extended Data Fig. 6b). The viscosity factor B (Extended Data Fig. 6c) is calculated using an empirical function, which is dependent on ice temperature (equation (6) in ref. ⁵⁷). Most surface fractures are 1-50m deep (less than 25% of the typical ice thickness), and the ice temperature within this range is approximately constant (figure. 1b in ref. ⁶²). Thus, we calculate B using the surface temperature T_s (Extended Data Fig. 6d), obtained from a time average of the regional climate model RACMO2.3p2. The negligible effect of vertical temperature gradient on the surface fracture stability is addressed in SI Section 7 and Extended Data Fig. 9. The fracture toughness is insensitive to temperature in the range of 100-273.15 K according to laboratory measurements (figure 3 in ref. ³⁶), and thus is assumed constant $K_{Ic} = 150$ kPa·m^{1/2} (ref. ³⁶) across ice-shelves in our study. Note that an alternative approach is to use the stresses computed directly by the model assimilation ref. ¹³. This has the advantage that the effects of ice damage (e.g. due to crevassing) are accounted for in the ice viscosity, but this does not impact our main conclusions (Extended Data Fig. 8).

3.2. Stability diagram for all ice-shelves and 2-D histogram

The axes of the fracture stability diagram (Fig. 3c) are dimensionless fracture toughness \tilde{K}_{Ic} and tensile resistive stress \tilde{R}_{xx} (equation 1), which controls whether fractures occur (equation 2) and their stability. To determine whether fractures form, \tilde{K}_{Ic} and \tilde{R}_{xx} are calculated on a 1 x 1 km grid using the datasets identified in the previous section. These values are plotted as red dots in Extended Data Fig. 7 ($n \approx 1.25 \times 10^6$ points), showing the range of parameter values across all ice shelves. The subset of locations where fractures are identified by the deep convolutional neural network (DCNN) are marked in yellow ($n \approx 32000$) in Extended Data Fig. 7. These points almost exclusively lie within the stable-fracture phase.

To visualize the density of points in Extended Data Fig. 7, we plot the 2-dimensional histogram for the fracture locations (yellow dots) in Fig. 3c in the main text. The data points are sorted into bins with logarithmically-varying widths for both axes (i.e. data in the range of $10^x - 10^{x+0.01}$ is sorted into the same bin). The total number of data points within each bin is denoted by the colour (Fig. 3c). This shows a dense population of fracture features within the parameter regime where we predict stable surface fractures and demonstrates a remarkable agreement with our analytical result (red line, equation 2) for the transition boundary between the no-surface-fracture and stable-surface-fracture regions of the stability diagram.

3.3. Uncertainties associated with our choices of stress and strain-rate fields

The tensile resistive stresses R_{xx} used in the stability diagram and vulnerability map in Fig. 3c and Fig. 4 are calculated from surface-temperature-dependent viscosity factor $B(T)$ and along-flow strain rate $\dot{\epsilon}_{xx}$ computed by Furst et al. (2016) (ref. ¹³). To check the sensitivity of our results to the strain rates, we repeat our analysis using along-flow strain rates supplied by ref. ⁶¹ (panel A). These strain rates were derived by applying Gaussian smoothing to the MEaSURES V2 Antarctic velocity product ^{60,63}. We find fewer points within the no-surface-fracture regime and an increase in the extent of the vulnerable regions (c.f. Extended Data Fig. 8a and Fig. 4a).

In addition, the impact of ice damage on ice viscosity⁶⁴ is neglected in the main text. More damaged ice is less viscous and therefore experiences less stress for a given strain rate. The stresses calculated by ref. ¹³ incorporate an inverted viscosity parameter, which is calculated so that model velocities match with observations⁶⁰. The effects of damage are therefore embedded in the computed stresses. Extended Data Fig. 8b and 9c show the stability diagram and vulnerability maps computed using the along-flow stress and 1st principal stress (i.e. maximal tensile resistive or minimal compressive stress) determined by ref. ¹³. The difference between the distribution of data within the stability diagram is small.

The conclusions drawn from our analysis of the stability diagram and vulnerability map are unaffected by these choices regarding strain-rates and stresses. First, most fracture features fall in the predicted physical regime (below the red theoretical curve). Second, large portions of the area vulnerable to hydrofracture (red regions in the lower panel) provide strong buttressing (outside the passive ice-shelf areas (blue)).

3.4. Advection of fractures and stress history

Although we evaluate the physical conditions (dimensionless stress and toughness; equations 1) at the present-day locations of the observed fractures, brittle fractures are likely to have initially formed

upstream of these locations and have been advected downstream. During this time they likely deformed viscously, causing the fracture to widen such that it can be seen in the 125m resolution satellite image. We track the stress upstream along streamlines (assuming steady flow) for all fracture features and identify the maximum dimensionless stress \tilde{R}_{xxmax} that the fracture has experienced since crossing the grounding line. For each fracture location detected by the DCNN, we then plot \tilde{R}_{xxmax} and the corresponding dimensionless toughness at the location where maximum dimensionless stress occurs, as shown in Extended Data Fig. 9b. Compared with \tilde{R}_{xx} and \tilde{K}_{Ic} evaluated at the locations of the fracture features, Extended Data Fig. 9a, the points evaluated at the locations of the maximum dimensionless stresses are shifted to the right, so are still in the physical regime where the theory predicts stable surface fractures. This shows that although brittle fractures can form upstream at higher stresses compared to their current locations, most of them (89%) remain in the physical regime where LEFM predicts stable surface fractures, after they are advected downstream to their current locations. Note that, from the MOA images we do not know exactly where or when each fracture initially forms, but we do know that the majority of the surface fractures experience physical conditions that allow brittle surface fracture both at their maximum stress in the past (Extended Data Fig. 9b) and their current stress state (Extended Data Fig. 9a). We thus use equation 2 (the analytical solution for the boundary between the no-surface-fracture/stable-surface-fracture regimes based on LEFM; red line in Extended Data Fig. 9) to estimate the areas where physical conditions allow the formation of dry, stable, and brittle surface fractures before they can later deform viscously and advect downstream. These areas are vulnerable to hydrofracture (red area in Fig. 4a) since water-filled fractures are unstable (from both LEFM and zero-stress approximation).

3.5. The surface expression of basal crevasses

As described in the main text, a subset of the fracture features identified by the DCNN could be surface expressions of basal crevasses³⁰⁻³². Although the DCNN was not trained to distinguish surface expressions of basal crevasses³⁰⁻³² from surface fractures, we note that the two features are not mutually exclusive and very often co-exist³¹ (to comprehensively distinguish these two features continent-wide radar profiles showing basal crevasse would be required). As noted by Bassis and Ma (2015)⁵⁸, a sufficiently wide basal crevasse can induce tensile stress near the surface large enough to create surface fractures. Most importantly, we show that most DCNN-identified fracture features (related to basal crevasses or not) occur where dimensionless stresses are sufficient to form stable dry surface fracture (Fig. 3c).

4. Lake locations

4.1 Stokes' supraglacial lake locations compared with vulnerability map

Stokes et al. (2019)²⁵ mapped supraglacial lakes in Landsat imagery from Jan 2017 across all East Antarctic ice shelves (defined using BedMap2's³⁷ ice shelf mask). Plotting their lake locations on our map of vulnerability to hydrofracture (Extended Data Fig. 10b-e), we see that they mostly lie in the resilient regions (yellow-green areas).

To obtain an upper estimate of the proportion of East Antarctic ice shelves that experience meltwater ponding and are vulnerable to hydrofracture, we sum the areas of the 1 km-by-1 km grid boxes that contain lakes and lie in the vulnerable regions, then divide by the total area of East Antarctic ice shelves, to give ~0.63%. The proportion of East Antarctic ice shelves that lie at the intersection of all three circles in Fig. 1 (i.e., meltwater ponds, they are vulnerable to hydrofracture and they provide significant buttressing) is approximately the same (~0.6%) because Stokes' lakes mostly lie in places providing significant buttressing (as identified by Fürst et al. (2016)¹³). Note that areas of most individual lakes are ~0.001-0.01 km² (see figure 3a in Stokes et al. (2019)²⁵) - much smaller than the spatial resolution (1 km²) of our vulnerability map. Thus the true overlaps between these regions may be 2-3 orders of magnitude smaller than estimated here.

Supplementary Information is available in the online version of the paper.

Acknowledgements We would like to thank Robin Bell, Ted Scambos, Ravindra Duddu and Brent Minchew for insightful discussions. We are grateful for the comments from the reviewers and editor, which helped to improve the manuscript. We also acknowledge the National Science Foundation for funding via Grant No. OPP-1743310. C.-Y.L. thanks Lamont-Doherty Earth Observatory for funding through the Lamont Postdoctoral Fellowship. J.M.W. acknowledges the Dutch Research Council (NWO) for funding through Veni Grant VI.Veni.192.083.

Author Contributions C.-Y.L. led the project and the preparation of the manuscript. C.-Y.L. and J.K. designed the research. M.W. helped with development of the research, contributed strain rate data and ideas related to buttressing. C.-Y.L. developed the fracture model and the stability diagram. P.-H.C.C. provided guidance regarding the selection and evaluation of machine learning models. C.-Y.L. conducted the machine-learning experiments and P.-H.C.C., P.G., and H.L. assisted with the employment of neural networks. J.S. prepared the Landsat images. J.M.W. provided RACMO2.3p2 climate model output. C.-Y.L. wrote the manuscript with help from J.K., M.W., and P.-H.C.C. and input from all authors. All authors contributed to discussions of the research.

Author Information Reprints and permissions information is available at www.nature.com/reprints. Readers are welcome to comment on the online version of the paper. Correspondence and requests for materials should be addressed to C.-Y.L. (cylai@ldeo.columbia.edu).

Competing Interests P.-H.C.C. is an employee of Google and owns Alphabet stock. Other authors declare no competing financial interests.

Disclaimer For P.-H.C.C., the work was done in personal time. The views expressed in this article are those of the authors and do not necessarily reflect the official policy or position of Google LLC.

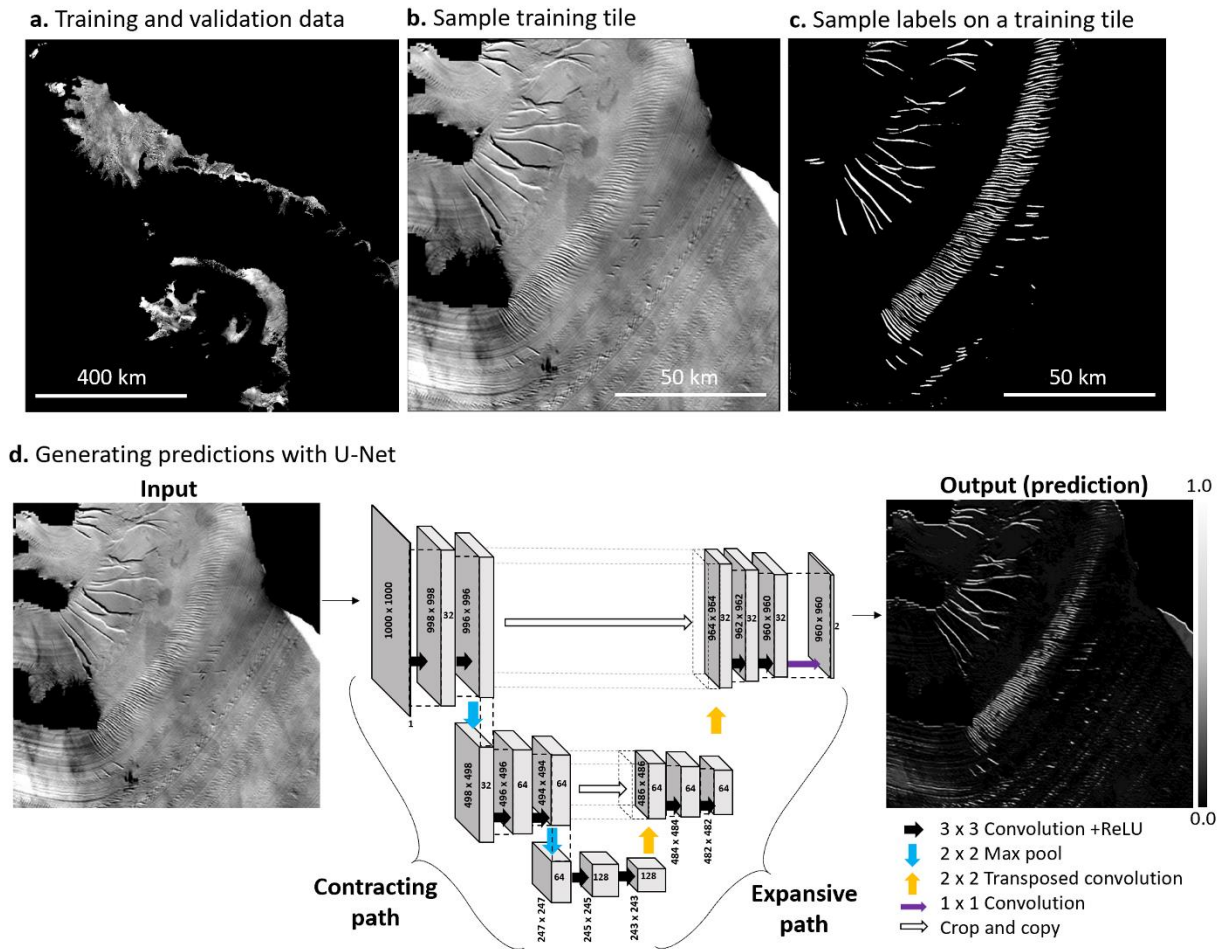
Code Availability

The code for our experiment is available at <https://github.com/chingyaolai/Antarctic-fracture-detection> (<http://doi.org/10.5281/zenodo.3899586>). The U-Net implementation is available at https://github.com/jakeret/tf_unet (ref. ⁶⁵). The FPN implementation is available at https://github.com/qubvel/segmentation_models (ref. ⁶⁶). The deep learning framework, TensorFlow, is available at <https://www.tensorflow.org/>. Scripts for calculating the fracture stability diagram (Fig. 3c) are available upon request.

Data Availability

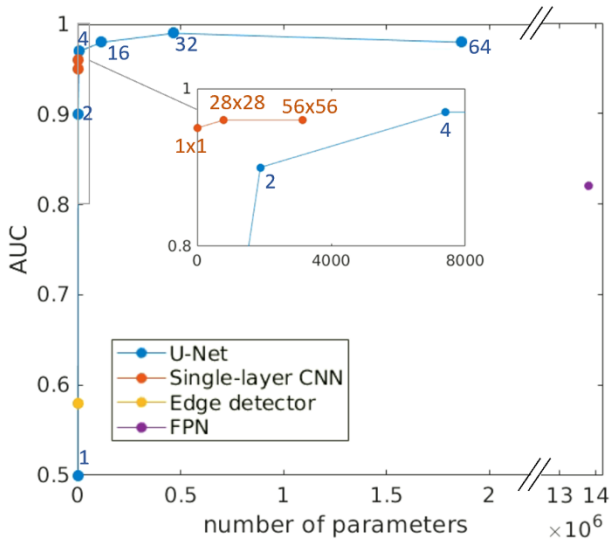
The training, validation, and testing datasets are available at <https://github.com/chingyaolai/Antarctic-fracture-detection> (<http://doi.org/10.5281/zenodo.3899586>). The neural-network mapped fracture locations on the MOA 2009 (125m resolution) imagery (Fig. 2) and the data required to construct the vulnerability map (Fig. 4) are available at <https://doi.org/10.15784/601335>. MOA (2009) imagery (<https://doi.org/10.7265/N5KP8037>) is available at the National Snow and Ice Data Center (NSIDC). Strain-rate fields are calculated from the dataset SUMER Antarctic Ice-shelf Buttressing, Version 1 (<https://doi.org/10.5067/FWHORAYVZCE7>), available at NSIDC. Ice-shelf thickness is from Bedmap2 (<https://www.bas.ac.uk/project/bedmap-2/>). The surface temperature data from the RACMO2.3p2 regional climate model are available from J.M.W. (j.m.vanwessem@uu.nl).

Extended Data Figures



Extended Data Figure 1 | Data preparation and the neural network architecture. The training and validation data are taken from a 8000 x 8000 pixel subset (covering Larsen and George VI ice shelves) of the 125m-resolution MODIS imagery, as shown in (a), which produces 32 tiles of 1000 x 1000 pixel images containing ice-shelves. The tiles are randomly separated into training (26 tiles) and validation (6 tiles) sets. (b) Example of a training tile and (c) the corresponding labels with white pixels indicating fractures. (d) U-Net architecture. The contracting and expansive paths give the U-Net²⁹ its U-shaped architecture. Arrows illustrate operations within the network and at each stage the data dimension is noted. The input image is 1000 x 1000 pixels with 1 channel and the output prediction of the U-Net contains two classes (fracture and non-fracture). The right panel shows the fracture predictions.

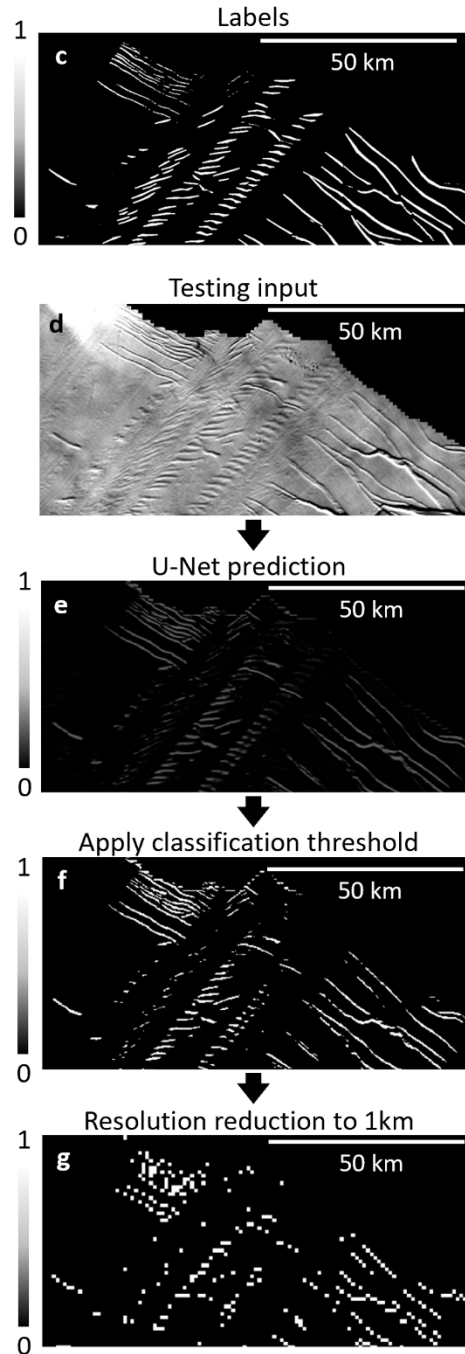
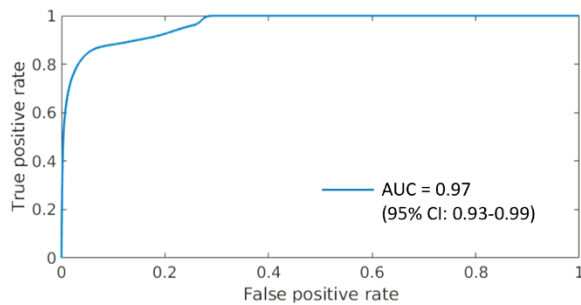
a. (i) Model comparison



(ii) AUC comparison

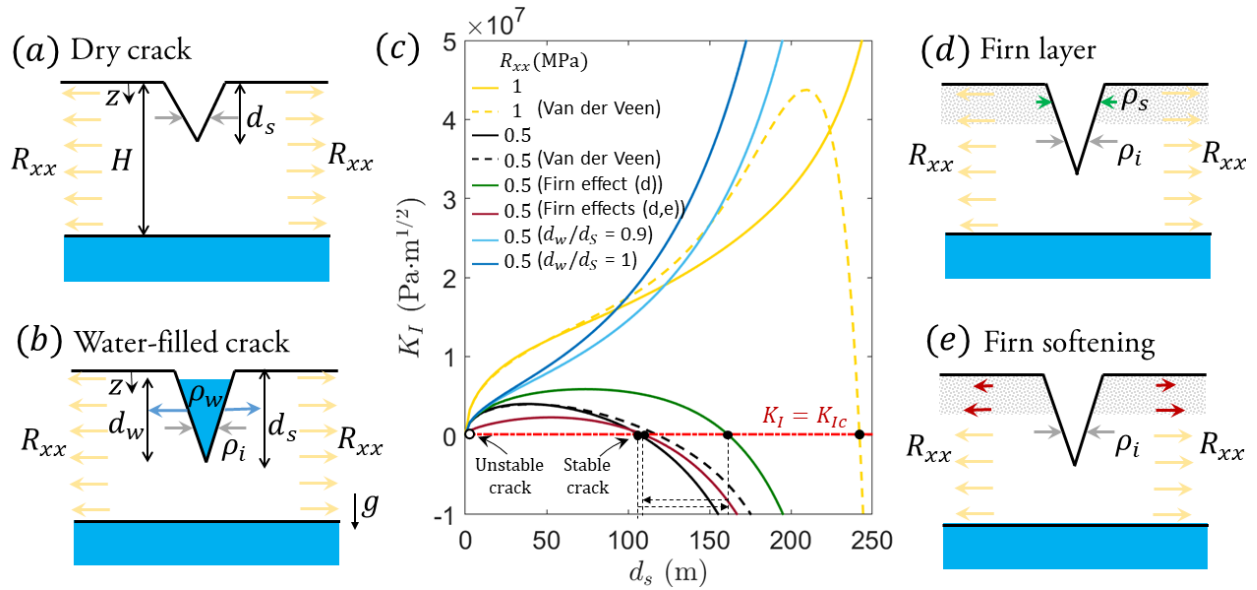
U-Net			Single-layer CNN			Edge detector		FPN	
d	N	AUC	k	N	AUC	N	AUC	N	AUC
1	490	0.50	1	2	0.95	0	0.58	13,809,092	0.82
2	1,886	0.90							
4	7,402	0.97	28	785	0.96				
16	116,770	0.98							
32	465,986	0.99	56	3,137	0.96				
64	1,861,762	0.98							

b. Performance on testing data

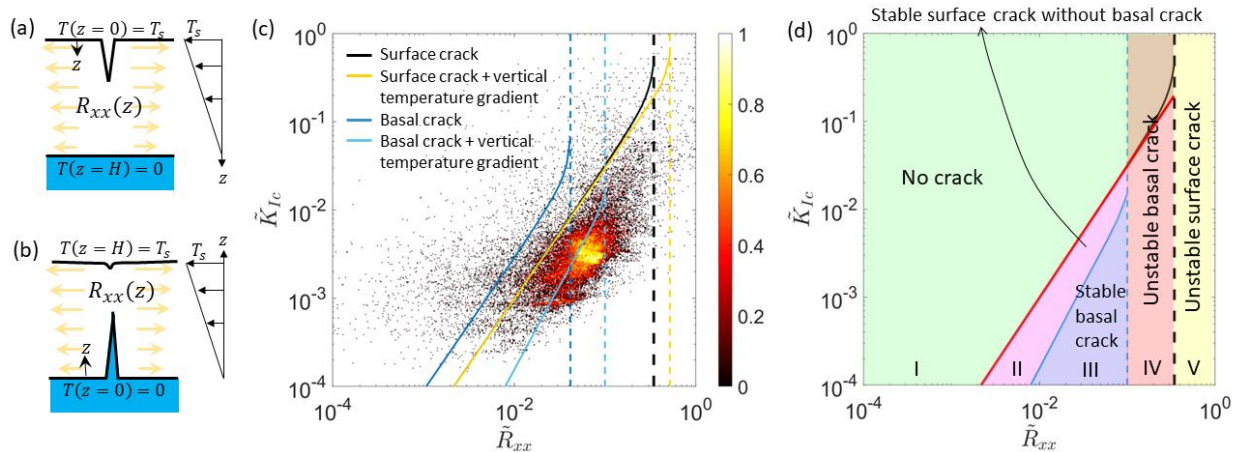


Extended Data Figure 2 | Performance of the DCNN and fracture classification. (a)(i) Comparisons of the area under the receiver operating characteristics curve (AUC) for the validation data over number of parameters (N) for an edge detector⁴⁴, single-layer CNN with different filter sizes (1×1 , 28×28 , 56×56 ; denoted by k in (a)(ii)), U-Net with different depths of first-layer feature maps (1, 2, 4, 16, 32, 64; denoted by d in (a)(ii)), and feature pyramid network (FPN)⁴³ using a ResNet-18 backbone. (a)(ii) The AUCs and number of parameters (N) of

each model evaluated against the validation data are summarized in the table. **(b)** The performance of the U-Net (with $d = 32$) evaluated against an unseen testing set is shown by the receiver operating characteristics (ROC) curves. An example of the validation label image and original MOA image are shown in **(c)** and **(d)**, respectively. **(e)** Output of the model, continuous values between 0 and 1. **(f)** Binarized classification of fractures that uses a threshold ($= 0.2$) maximizing the F1 score on the validation set. Fracture features with predictions exceeding the threshold are marked white. **(g)** The resolution of the fracture map is reduced to 1 km, the resolution of the strain-rate data, before we incorporate the DCNN result with other data in Extended Data Fig. 6.



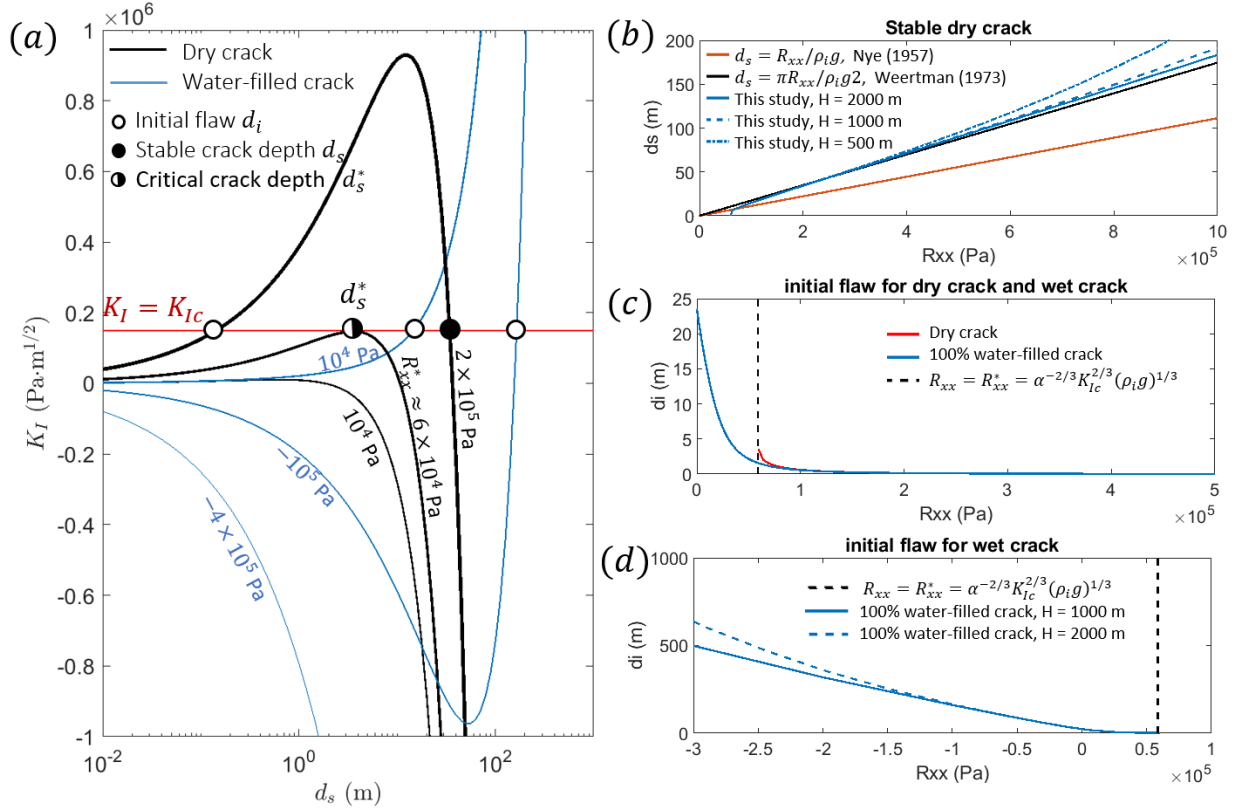
Extended Data Figure 3 | Stresses acting on a surface fracture and fracture stability. (a) and (b) illustrate the effects of tensile resistive stress, hydrostatic stress of water, and overburden stress of ice on opening or closing of a surface fracture. (c) The stress intensity factor (K_I) as a function of surface fracture depth (d_s) (equation (M5)) computed with $R_{xx} = [0.5, 1]$ MPa, $H = 300$ m, surface firm density $\rho_s = 400 \text{ kg m}^{-3}$, and $C = 0.02 \text{ m}^{-1}$ (see equation (M6); ref. ²). (The solution derived in this work is shown with a solid curves and that of Van der Veen (ref. ²) by dashed curves.) The additional impacts of a firm layer are due to (d) reduced density and (e) reduced viscosity. Reduced overburden stress due to lower density firm compared to ice acts to deepen surface fractures (black dot on green curve in (c)). In contrast, the reduced tensile resistive stress due to the reduced firm viscosity reduces surface fracture depth. The net effects from firm, shown by the red curve in (c), are secondary compared with the effects from tensile resistive and overburden stresses of ice. Therefore in the main analysis we neglect the effect of firm.



	(e) Furst's strain rate + B(T)	(f) Wearing's strain rate and B(T)	(g) Furst's along-flow stress	(h) Furst's 1 st principal stress
I	27%	22%	34%	19%
II	21%	21%	26%	28%
III	53%	62%	41%	50%
IV	4%	3%	2%	3%
V	0.4%	0.5%	0.1%	0.2%

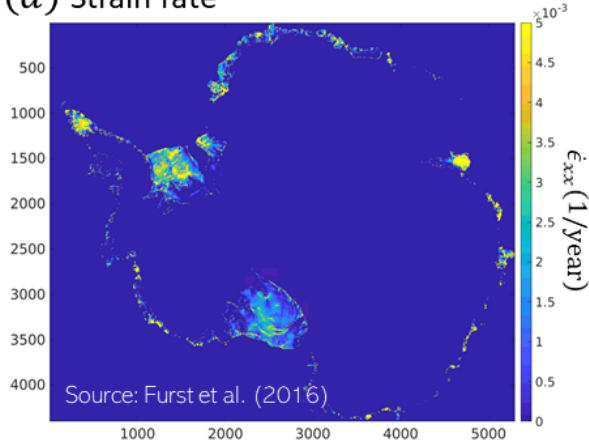
Extended Data Figure 4 | Physical regimes of surface and basal fractures. The schematics of (a) surface and (b) basal crevasse with depth varying resistive stress $R_{xx}(z)$ due to the vertical temperature gradient (assumed linear). (c) The fracture stability diagram for surface and basal crevasses with and without temperature effects (assuming the surface and the base of ice shelf are -30 and 0 °C, respectively). Dashed and solid lines represent the transition boundaries of stable-to-unstable and no crack-to-stable crack, respectively. Warmer ice at the base reduces the ice viscosity (and thus stress), which impacts the locations of the stability boundaries of basal crevasse. (d) The five physical regimes (I-V) defined by the transition boundaries for surface crevasse (black curves in (c)) and basal crevasse with temperature effects (light blue curves in (c)). (e-h) The locations corresponding to regimes I-V on ice shelves are determined by different estimates of stress. The percentage values denote the portion of ice-shelf area containing the physical condition in each regime (I-V). The green, pink, blue,

red, yellow, and white areas correspond to regimes I, II, III, IV, V, and the U-Net-detected fracture locations, respectively. First and second columns correspond to the stress field determined by the temperature dependent viscosity factor $B(T)$ (equation (6) in ref.⁴⁷) combined with along-flow strain rates obtained by **(e)** Fürst et al. (2016) (ref.¹³) and **(f)** Wearing (2017) (ref.⁴⁶). The stress field in the **(g)** along-flow and **(h)** and 1st principal stresses direction calculated by ref.¹³ include the effects of damage-induced ice softening through the data assimilation and model inversion process. The second row of **(e-h)** is the close view of the white box in the first row. Note that the spatial areas of regimes I-V are calculated based solely on the dimensionless stress and toughness, and are independent of the U-Net result. The spatial resolution is 1km, same as the stress field resolution used in ref.¹³.

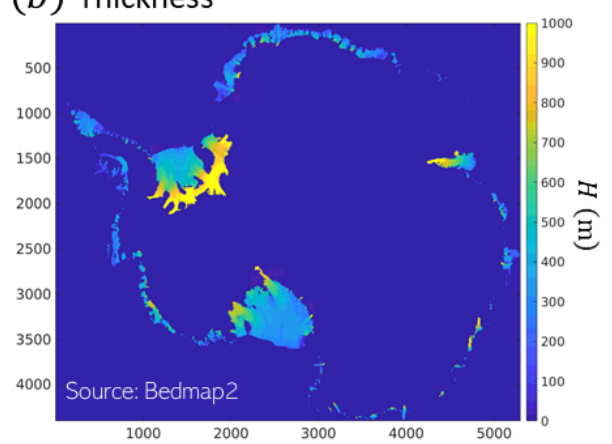


Extended Data Figure 5 | Comparison between dry and water-filled fractures in LEFM (a) The stress intensity factor (equation (M5)) as a function of surface fracture depth is calculated for hydrofractures (blue curves) and dry surface fractures (black curves) for ice thickness $H=1000$ m. The number alongside each curve is the corresponding tensile resistive stress, R_{xx} . Above the critical stress $R_{xx}^* \approx 60$ kPa (calculated using equation 2 and $K_{Ic} \approx 150$ kPa·m^{1/2}) dry-surface-fracture depths are stable (d_s black dot). Hydrofractures can become unstable when a pre-existing flaw filled with water reaches a depth denoted by the white dots (d_i). Water-filled initial flaws smaller than the required depth d_i will remain closed. When stress is sufficiently compressive, water-filled fractures will not grow (e.g., the blue curve has negative slopes for any surface fracture depth below the red line). (b) Comparison of stable dry-surface-fracture depth d_s with previous theories. Our numerical solution approaches Weertman's solution at large ice thickness. (c, d) The required depth of an initial flaw, d_i , to destabilize a hydrofracture as a function of stress is shown by blue curves. The pre-existing flaw depths required to initialize stable dry surface fractures are plotted as a red curve in (c), and reach a maximum of ~ 3.8 m at the critical stress R_{xx}^* (dashed line). Note that at the critical stress R_{xx}^* the required initial flaw depth is the same as fracture depth, i.e. $d_i = d_s = d_s^* \approx 3.8$ m (half-white half-black dot in (a)).

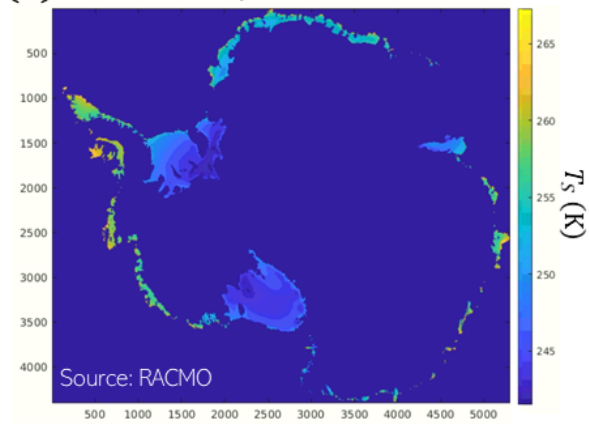
(a) Strain rate



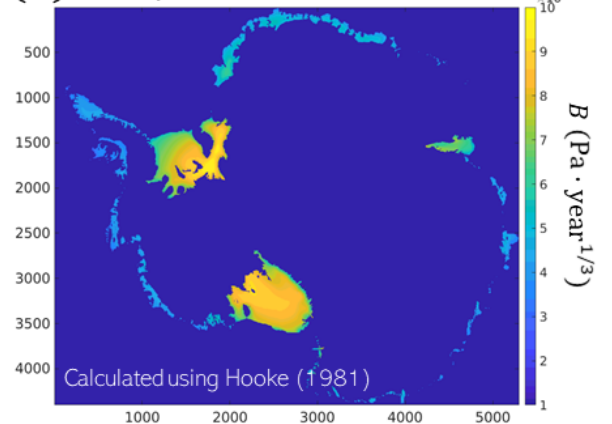
(b) Thickness



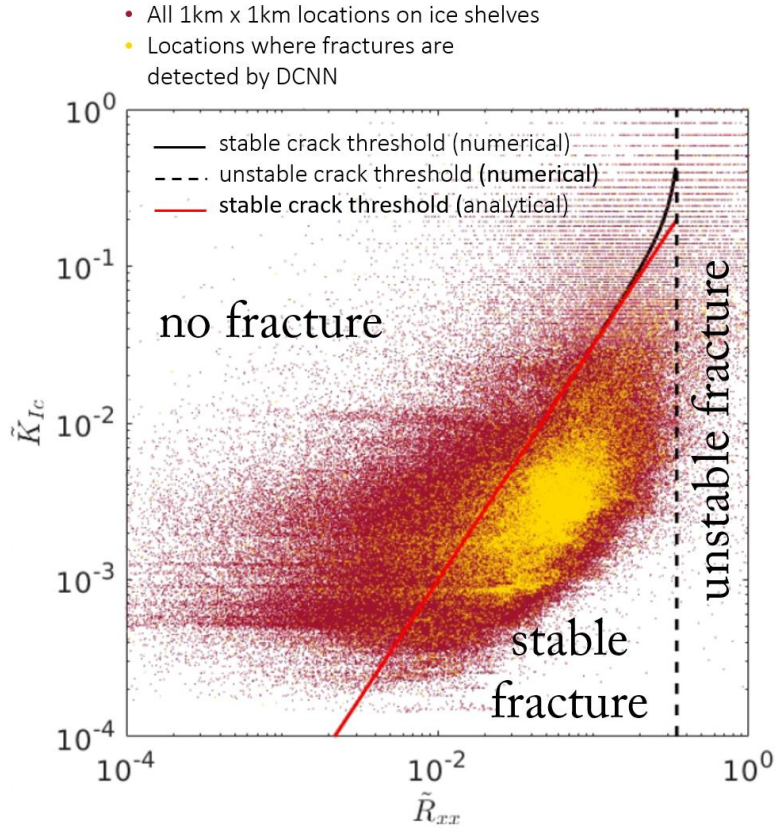
(c) Surface temperature



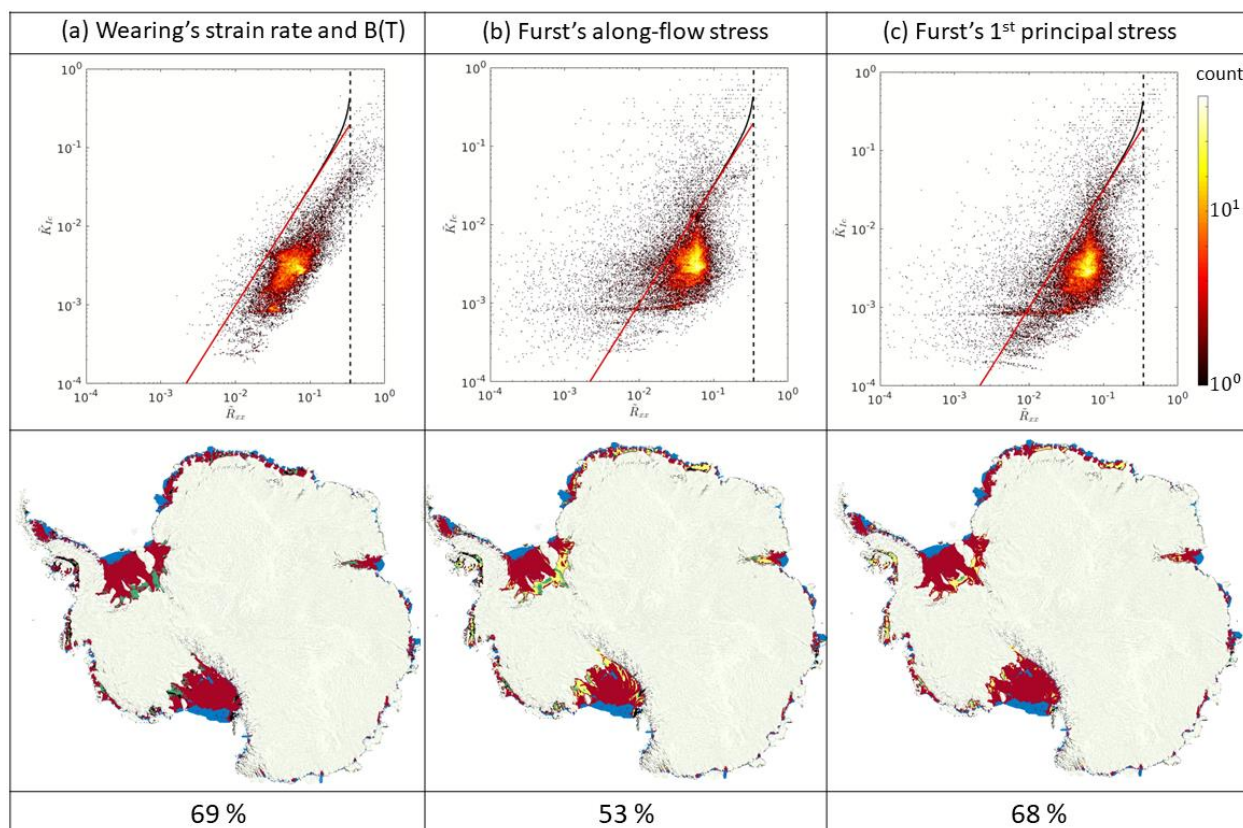
(d) Flow parameter



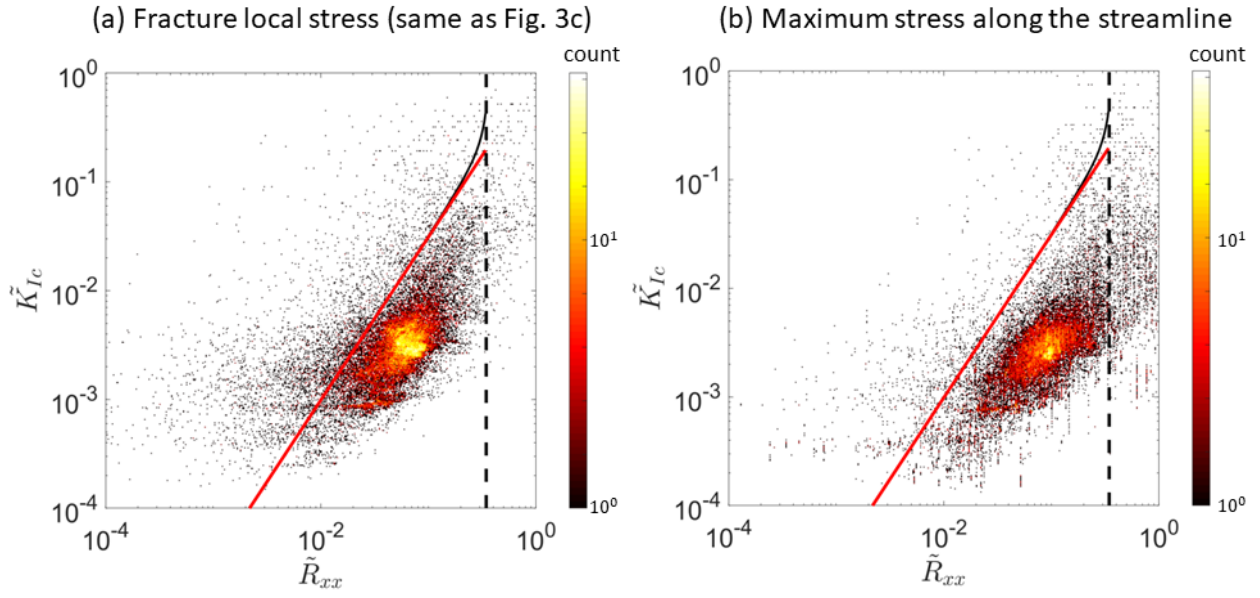
Extended Data Figure 6 | Antarctic-wide data used to predict vulnerability to hydrofracture. The dimensionless toughness and dimensionless stress are evaluated using (a) strain rates, (b) ice-shelf thickness, (c) surface temperature and (d) viscosity factor B (calculated from surface temperature), and plotted on the fracture stability diagram (Fig. 3c).



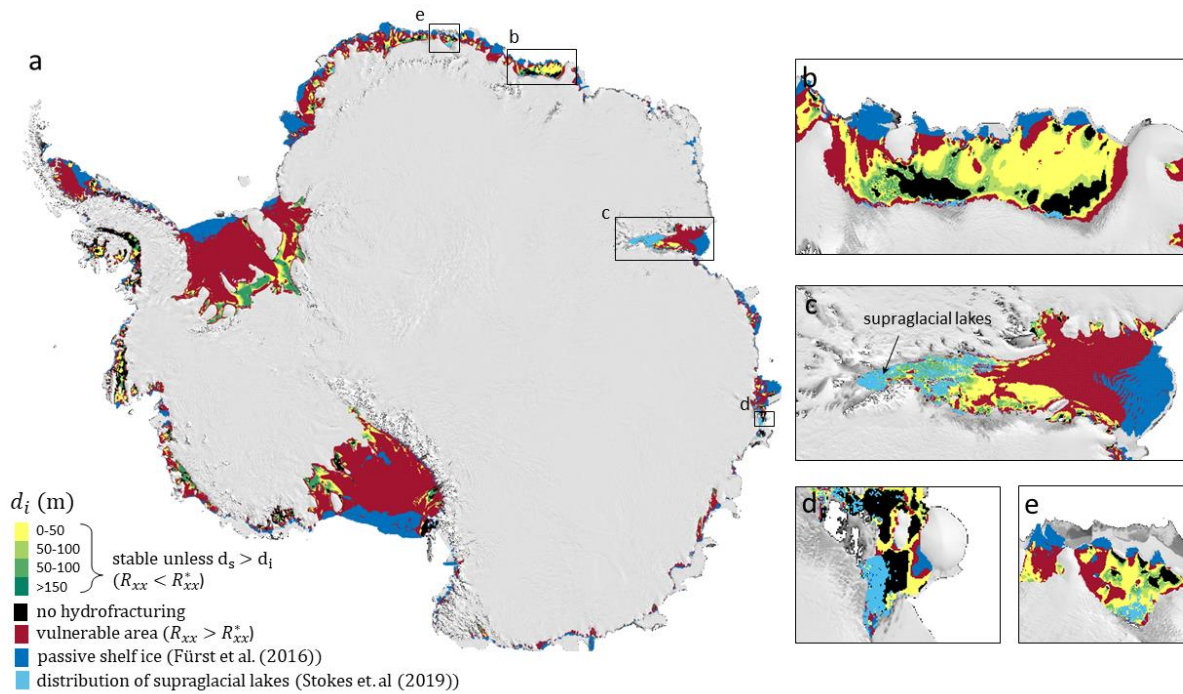
Extended Data Figure 7 | Surface fracture stability diagram. The two parameters determining fracture stability, \tilde{K}_{Ic} and \tilde{R}_{xx} , are computed at every 1x 1 km location on all ice shelves marked as red ($n \approx 1.25$ million points) and all fracture features detected by the DCNN marked as yellow dots ($n \approx 32000$). The frequency distribution of the yellow points is shown in Fig. 3c.



Extended Data Figure 8 | Alternative stress computations. Sensitivity of surface fracture stability diagram (upper row) and the vulnerability map (lower row) to choices of stress and strain-rate data. The results are computed using strain rate calculated by ref. ⁴⁶ (a), along-flow stress (b) and 1st principal stresses (c) both from ref. ¹³, which include damage-induced ice softening. Colour scale for the lower panel is the same as Fig. 4. The percentage values in the bottom row denotes the percentage of the total ice shelf area that is in the red regime in the second row (i.e. both buttressed and vulnerable to hydrofracture). Our main conclusions - ice-shelf stresses closely agree with the fracture criteria, and large buttressed areas are vulnerable to hydrofracture - are not affected by the use of these alternative stress fields.



Extended Data Figure 9 | Advection of fracture and stress history. We track the resistive stress upstream along streamlines (assuming steady-state) and identify the maximum dimensionless stress \tilde{R}_{xxmax} each fracture feature has experienced in the past. For each location identified as a fracture by the DCNN, we evaluate \tilde{R}_{xxmax} and the corresponding dimensionless toughness \tilde{K}_{Ic} at the location where maximum dimensionless stress occurs, as shown in (b). The dimensionless parameters \tilde{R}_{xx} and \tilde{K}_{Ic} evaluated directly at the locations of fracture features are shown in (a) (same as Fig. 3c) for comparison. (b) The maximum dimensionless stresses mostly fracture features exceed the threshold for surface fracture formation (red line; equation 2).



Extended Data Figure 10 | East Antarctic lake locations compared with vulnerability map. Stokes et al. (2019)²⁴ have mapped lakes across much of East Antarctica for one melt season (2017), enabling us to compare these locations to our vulnerability map (Fig. 4). We find that very little vulnerable and buttressing area contain lakes today on East Antarctic ice shelves. An upper estimate of the overlap between “lake-covered area” (top circle of Fig. 1) and “stress state-related vulnerable area” (lower left circle of Fig. 1) is only ~0.63% of the East Antarctic ice-shelf area.

References

1. Weertman, J. Can a water-filled crevasse reach the bottom surface of a glacier. *IASH publ* **95**, 139–145 (1973).
2. van der Veen, C. J. Fracture mechanics approach to penetration of surface crevasses on glaciers. *Cold Reg. Sci. Technol.* **27**, 31–47 (1998).
3. Benn, D. I., Warren, C. R. & Mottram, R. H. Calving processes and the dynamics of calving glaciers. *Earth-Sci. Rev.* **82**, 143–179 (2007).
4. Scambos, T. *et al.* Ice shelf disintegration by plate bending and hydro-fracture: Satellite observations and model results of the 2008 Wilkins ice shelf break-ups. *Earth Planet. Sci. Lett.* **280**, 51–60 (2009).
5. Banwell, A. F., MacAyeal, D. R. & Sergienko, O. V. Breakup of the Larsen B Ice Shelf triggered by chain reaction drainage of supraglacial lakes. *Geophys. Res. Lett.* **40**, 5872–5876 (2013).
6. Jiménez, S. & Duddu, R. On the evaluation of the stress intensity factor in calving models using linear elastic fracture mechanics. *J. Glaciol.* **64**, 759–770 (2018).
7. Alley, K. E., Scambos, T. A., Miller, J. Z., Long, D. G. & MacFerrin, M. Quantifying vulnerability of Antarctic ice shelves to hydrofracture using microwave scattering properties. *Remote Sens. Environ.* **210**, 297–306 (2018).
8. Rack, W. & Rott, H. Pattern of retreat and disintegration of the Larsen B ice shelf, Antarctic Peninsula. *Ann. Glaciol.* **39**, 505–510 (2004).
9. Pollard, D., DeConto, R. M. & Alley, R. B. Potential Antarctic Ice Sheet retreat driven by hydrofracturing and ice cliff failure. *Earth Planet. Sci. Lett.* **412**, 112–121 (2015).
10. DeConto, R. M. & Pollard, D. Contribution of Antarctica to past and future sea-level rise. *Nature* **531**, 591–597 (2016).
11. Schoof, C. Ice sheet grounding line dynamics: Steady states, stability, and hysteresis. *Journal of Geophysical Research: Earth Surface* **112**, (2007).

12. Gudmundsson, G. H. Ice-shelf buttressing and the stability of marine ice sheets. *The Cryosphere Discussions* vol. 6 3937–3962 (2012).
13. Fürst, J. J. *et al.* The safety band of Antarctic ice shelves. *Nat. Clim. Chang.* **6**, 479–482 (2016).
14. Rignot, E. Accelerated ice discharge from the Antarctic Peninsula following the collapse of Larsen B ice shelf. *Geophys. Res. Lett.* **31**, 959 (2004).
15. Scambos, T. A. Glacier acceleration and thinning after ice shelf collapse in the Larsen B embayment, Antarctica. *Geophys. Res. Lett.* **31**, 1560 (2004).
16. Wuite, J. *et al.* Evolution of surface velocities and ice discharge of Larsen B outlet glaciers from 1995 to 2013. *The Cryosphere Discussions* vol. 8 6271–6301 (2014).
17. Trusel, L. D. *et al.* Divergent trajectories of Antarctic surface melt under two twenty-first-century climate scenarios. *Nat. Geosci.* **8**, 927 (2015).
18. van der Veen, C. J. & Whillans, I. M. Force Budget: I. Theory and Numerical Methods. *J. Glaciol.* **35**, 53–60 (1989).
19. Reese, R., Gudmundsson, G. H., Levermann, A. & Winkelmann, R. The far reach of ice-shelf thinning in Antarctica. *Nat. Clim. Chang.* **8**, 53–57 (2017).
20. Robel, A. A. & Banwell, A. F. A Speed Limit on Ice Shelf Collapse Through Hydrofracture. *Geophys. Res. Lett.* **46**, 12092–12100 (2019).
21. MacAyeal, D. R., Sergienko, O. V. & Banwell, A. F. A model of viscoelastic ice-shelf flexure. *Journal of Glaciology* vol. 61 635–645 (2015).
22. Banwell, A. F., Willis, I. C., Macdonald, G. J., Goodsell, B. & MacAyeal, D. R. Direct measurements of ice-shelf flexure caused by surface meltwater ponding and drainage. *Nature Communications* vol. 10 (2019).
23. Kingslake, J., Ely, J. C., Das, I. & Bell, R. E. Widespread movement of meltwater onto and across Antarctic ice shelves. *Nature* **544**, 349–352 (2017).
24. Bell, R. E. *et al.* Antarctic ice shelf potentially stabilized by export of meltwater in surface river. *Nature* **544**, 344–348 (2017).

25. Stokes, C. R., Sanderson, J. E., Miles, B. W. J., Jamieson, S. S. R. & Leeson, A. A. Widespread distribution of supraglacial lakes around the margin of the East Antarctic Ice Sheet. *Sci. Rep.* **9**, 13823 (2019).
26. Kingslake, J., Trusel L.D., Banwell A., Bell R.E., Das I., DeConto R.M., Tedesco M., Lenaerts J.T.M., Schoof C. Report on Antarctic surface hydrology workshop, LDEO. in (USAP-DC, 2018). doi:10.15784/601170.
27. Munneke, P. K., Ligtenberg, S. R. M., Van Den Broeke, M. R. & Vaughan, D. G. Firn air depletion as a precursor of Antarctic ice-shelf collapse. *J. Glaciol.* **60**, 205–214 (2014).
28. Haran, T., Bohlander, J., Scambos, T., Painter, T. & Fahnestock, M. MODIS Mosaic of Antarctica 2008--2009 (MOA2009) image map. *Boulder, Colorado USA, National Snow and Ice Data Center* **10**, N5KP8037 (2014).
29. Ronneberger, O., Fischer, P. & Brox, T. U-Net: Convolutional Networks for Biomedical Image Segmentation. in *Medical Image Computing and Computer-Assisted Intervention – MICCAI 2015* 234–241 (Springer International Publishing, 2015).
30. McGrath, D. *et al.* Basal crevasses on the Larsen C Ice Shelf, Antarctica: Implications for meltwater ponding and hydrofracture. *Geophysical Research Letters* vol. 39 (2012).
31. McGrath, D. *et al.* Basal crevasses and associated surface crevassing on the Larsen C ice shelf, Antarctica, and their role in ice-shelf instability. *Ann. Glaciol.* **53**, 10–18 (2012).
32. Luckman, A. *et al.* Basal crevasses in Larsen C Ice Shelf and implications for their global abundance. *The Cryosphere* **6**, 113–123 (2012).
33. Nye, J. F. The distribution of stress and velocity in glaciers and ice-sheets. *Proc. R. Soc. Lond. A Math. Phys. Sci.* **239**, 113–133 (1957).
34. van der Veen, C. J. Fracture mechanics approach to penetration of bottom crevasses on glaciers. *Cold Reg. Sci. Technol.* **27**, 213–223 (1998).
35. Duddu, R., Jiménez, S. & Bassis, J. A non-local continuum poro-damage mechanics model for hydrofracturing of surface crevasses in grounded glaciers. *J. Glaciol.* **66**, 415–429 (2020).

36. Litwin, K. L., Zygielbaum, B. R., Polito, P. J., Sklar, L. S. & Collins, G. C. Influence of temperature, composition, and grain size on the tensile failure of water ice: Implications for erosion on Titan. *Journal of Geophysical Research: Planets* **117**, (2012).
37. Fretwell, P. *et al.* Bedmap2: improved ice bed, surface and thickness datasets for Antarctica. *improved ice bed, surface and thickness datasets for Antarctica, The Cryosphere* **7**, 393 (2013).
38. van Wessem, J. M. *et al.* Modelling the climate and surface mass balance of polar ice sheets using RACMO2 – Part 2: Antarctica (1979–2016). *The Cryosphere* vol. 12 1479–1498 (2018).
39. Poinar, K. *et al.* Drainage of Southeast Greenland Firn Aquifer Water through Crevasses to the Bed. *Front. Earth Sci.* **5**, 8 (2017).
40. Lenaerts, J. T. M. *et al.* Meltwater produced by wind–albedo interaction stored in an East Antarctic ice shelf. *Nat. Clim. Chang.* **7**, 58 (2016).
41. Bell, R. E., Banwell, A. F., Trusel, L. D. & Kingslake, J. Antarctic surface hydrology and impacts on ice-sheet mass balance. *Nat. Clim. Chang.* **1** (2018).
42. Scambos, T. A., Haran, T. M., Fahnestock, M. A., Painter, T. H. & Bohlander, J. MODIS-based Mosaic of Antarctica (MOA) data sets: Continent-wide surface morphology and snow grain size. *Remote Sens. Environ.* **111**, 242–257 (2007).
43. Lin, T.-Y. *et al.* Feature pyramid networks for object detection. in *Proceedings of the IEEE conference on computer vision and pattern recognition* 2117–2125 (2017).
44. Canny, J. A computational approach to edge detection. *IEEE Trans. Pattern Anal. Mach. Intell.* **8**, 679–698 (1986).
45. Chen, L.-C., Zhu, Y., Papandreou, G., Schroff, F. & Adam, H. Encoder-Decoder with Atrous Separable Convolution for Semantic Image Segmentation. *Computer Vision – ECCV 2018* 833–851 (2018) doi:10.1007/978-3-030-01234-2_49.
46. Badrinarayanan, V., Kendall, A. & Cipolla, R. SegNet: A Deep Convolutional Encoder-Decoder Architecture for Image Segmentation. *IEEE Transactions on Pattern Analysis and Machine Intelligence* vol. 39 2481–2495 (2017).

47. Zhao, H., Shi, J., Qi, X., Wang, X. & Jia, J. Pyramid scene parsing network. in *Proceedings of the IEEE conference on computer vision and pattern recognition* 2881–2890 (2017).
48. Lin, T.-Y. *et al.* Microsoft COCO: Common Objects in Context. in *Computer Vision – ECCV 2014* 740–755 (Springer International Publishing, 2014).
49. Fahnestock, M. *et al.* Rapid large-area mapping of ice flow using Landsat 8. *Remote Sens. Environ.* **185**, 84–94 (2016).
50. Rignot, E., Echelmeyer, K. & Krabill, W. Penetration depth of interferometric synthetic-aperture radar signals in snow and ice. *Geophys. Res. Lett.* **28**, 3501–3504 (2001).
51. Gray, L., Conway, H., King, E. & Smith, B. Flow stripes, GPR stratigraphy and RADARSAT imagery. *J. Glaciol.* **54**, 936–938 (2008).
52. Irwin, G. R. Analysis of stresses and strains near the end of a crack traversing a plate. *J. Appl. Mech.* **24**, 361–364 (1957).
53. H. Tada, P. C. P. & Irwin, G. R. The stress analysis of cracks handbook. 3rd ed. *Professional Engineering Publishing* (2000).
54. Gagliardini, O. & Meyssonier, J. Flow simulation of a firn-covered cold glacier. *Ann. Glaciol.* **24**, 242–248 (1997).
55. van der Veen, C. J. *Fundamentals of glacier dynamics*. (CRC press, 2013).
56. Griffith, A. A. The Phenomena of Rupture and Flow in Solids. *Philosophical Transactions of the Royal Society A: Mathematical, Physical and Engineering Sciences* vol. 221 163–198 (1921).
57. LeB. Hooke, R. Flow law for polycrystalline ice in glaciers: Comparison of theoretical predictions, laboratory data, and field measurements. *Rev. Geophys.* **19**, 664 (1981).
58. Bassis, J. N. & Ma, Y. Evolution of basal crevasses links ice shelf stability to ocean forcing. *Earth Planet. Sci. Lett.* **409**, 203–211 (2015).
59. Durand, G., F. Gillet-Chaulet, O. Gagliardini, J. J. Fürst. SUMER Antarctic Ice-shelf Buttressing, Version 1. *Boulder, CO: NASA DAAC at the National Snow and Ice Data Center*
doi:10.5067/FWHORAYVZCE7.

60. Rignot, E., Mouginot, J. & Scheuchl, B. Ice flow of the Antarctic ice sheet. *Science* **333**, 1427–1430 (2011).
61. Wearing, M. The flow dynamics and buttressing of ice shelves. (University of Cambridge, 2017).
62. Rezvanbehbahani, S., Veen, C. J. & Stearns, L. A. An Improved Analytical Solution for the Temperature Profile of Ice Sheets. *J. Geophys. Res. Earth Surf.* **124**, 271–286 (2019).
63. Rignot, E., Mouginot, J. & Scheuchl, B. MEaSURES InSAR-based Antarctica ice velocity map, version 2. Boulder, CO: NASA DAAC at the National Snow and Ice Data Center (2017) doi:10.5067/D7GK8F5J8M8R.
64. Borstad, C. *et al.* A constitutive framework for predicting weakening and reduced buttressing of ice shelves based on observations of the progressive deterioration of the remnant Larsen B Ice Shelf. *Geophys. Res. Lett.* **43**, 2027–2035 (2016).
65. Akeret, J., Chang, C., Lucchi, A. & Refregier, A. Radio frequency interference mitigation using deep convolutional neural networks. *Astronomy and Computing* **18**, 35–39 (2017).
66. Yakubovskiy, P. Segmentation models. *GitHub repository* (2019).